**NASA DEVELOP National Program**
**Pop-Up Project**

*Spring 2024*

# Central California Disasters

## Incorporating Satellite-Derived Precipitation and Soil Moisture Products into Flood Preparedness and Emergency Management in California

**DEVELOP Technical Report**
March 29th, 2024


Abhinav Banthiya (Project Lead)
Chanice Brown
Jan Hery
Shagun Sengupta

***Advisor:***
Dr. Venkat Lakshmi, University of Virginia (Science Advisor)

***Lead:***
Isabel Lubitz (Maryland – Goddard)

# 1. Abstract

Atmospheric rivers are a major contributor to extreme precipitation events and flooding in California. This study assessed the feasibility of using Earth observation data to monitor precipitation, soil moisture, and flooding from atmospheric rivers in the Salinas River Watershed in central California during the winter of 2022-2023. The team analyzed satellite derived precipitation estimates from the Global Precipitation Measurement mission, soil moisture data from the Soil Moisture Active Passive radiometer, and synthetic aperture radar imagery from Sentinel-1 to detect flood inundation. Global Precipitation Measurement precipitation estimates were found to underestimate rainfall by 33% to 52% compared to rain gauge data. The team found the Soil Moisture Active Passive dataset to be a valuable flooding indicator that they could visualize through various graphical representations, although its accuracy still needs verification with in-situ flood maps. Sentinel-1 synthetic aperture radar imagery provided mapping of flood inundation extent along the Salinas River and surrounding areas and the Blue Spot model appears to be a good predictor of pluvial flood zones. The findings suggest Earth observations can enhance precipitation and flooding monitoring by the California Department of Water Resources, though further verification is needed. Integration of these datasets with vulnerability indices highlighted communities at highest risk during the 2022-2023 flooding events.



**Key Terms**

California atmospheric rivers, pluvial flooding, Earth observations, GPM IMERG, SMAP, Sentinel-1, SAR, Precipitation, Soil Moisture, Flood Inundations, Community Vulnerability.


# 2. Introduction

### *2.1 Background Information*

California experienced major storms and rainfall caused by multiple Atmospheric Rivers (ARs) in late 2022 through early 2023, resulting in major flooding, 22 lives lost, and 4.6 billion dollars in property damage across the state (Smith et al., 2024). An AR is a narrow corridor of concentrated moisture in the atmosphere that can transport large amounts of water vapor over long distances, often resulting in intense precipitation events when it makes landfall. This project partnered with the California Department of Water Resources (CA DWR) to assess the feasibility of using satellite data for monitoring precipitation and soil moisture to fill in data gaps and improve risk assessments in Central California. The team used the 2022-2023 winter storms and flooding events in the Salinas River Watershed as a case study for the potential utility of these datasets to inform flooding preparedness and emergency management efforts.

Although the CA DWR has access to in-situ data along with ground personnel to manage flood events, they have certain data gaps. They use radar and rain gauge data points for their hydrological flood modeling, such as the National Oceanic and Atmospheric Administration's (NOAA) California Nevada River Forecast Center and rain gauges to produce data for meteorological modeling. However, the rain gauges are sparsely located in the Salinas River Watershed and the basin conditions of the watershed that contribute to flooding are still not accurately measured with NOAA's data. The CA DWR also does not use any soil moisture data in their model. As such, the team aimed to explore rainfall and soil moisture data from Earth observations to fill these data gaps.

### 2.2 Atmospheric Rivers

ARs are elongated bands of concentrated moisture that occur in the Earth's atmosphere. They play a critical role in the planet's water cycle by transporting large amounts of water vapor from the tropics to higher latitudes, influencing weather and climate patterns significantly (Gimeno et al., 2014). ARs typically form in the subtropical regions of the Earth's atmosphere, where warm temperatures cause ocean water to evaporate and rise into the atmosphere and are driven by the jet stream at high altitudes. They can extend for thousands of kilometers and are often several hundred kilometers wide. As this moist air is transported poleward, it can lead to heavy precipitation when it encounters landmasses or interacts with other weather systems (Gimeno et al., 2014). AR-related flooding is primarily caused by intense rainfall. When an AR makes landfall or interacts with

a stationary weather system, it can result in prolonged and heavy precipitation and overwhelm drainage systems, saturate soils, and lead to rapid runoff. Therefore, AR events can lead to pluvial flooding, which is a type of flooding caused by intense rainfall and can happen independently of an existing water body.

Understanding the impact of ARs on heavy rainfall and flooding is crucial for effective flood preparedness and emergency management. ARs, along with orographic enhancement and strong winds, are identified as pivotal factors influencing the intensity of heavy rainfall and flooding (Ralph et al., 2003). Moreover, Nieman et al. (2008) utilized a combination of satellite and ground-based data to demonstrate that, particularly in California, ARs yield twice as much precipitation as all other types of storms. Guan et al. (2010) noted that approximately 40% of the annual snow accumulation in California's Sierra Nevada region occurs during AR events spanning the water years from 2004 to 2010. Additionally, Wen et al. (2018) identified that precise quantification of extreme precipitation linked to ARs across various spatial and temporal scales holds immense value for numerous applications. Furthermore, Earth observation data offers considerable temporal and spatial resolutions that can be utilized for flood monitoring (Friedrich et al., 2024). Therefore, in this project the team used Earth observations, especially sensors that can estimate precipitation and soil moisture, to examine the feasibility of monitoring flood risks during AR events in California.

### *2.2 Study Area and Period*

During the 2022-2023 AR events, the integrated water vapor transport, a measurement of wind speed and atmospheric moisture used to approximate the intensity of AR events, ranged from 300 to 500 percent more than normal throughout California, with the highest percentages found in the Central Valley. Within the Central Valley, the CA DWR identified the Salinas River Watershed as their focus region because it is agriculturally rich and houses some of the most vulnerable communities in California.

For the analysis, the team examined all major AR events leading to flooding during the Winter of 2022-2023. Six distinct flooding events occurred in Monterey County, California from December 2022 to March 2023. These events were identified using the Storm Events database, managed by NOAA. In order to capture changes in soil moisture conditions before and after the major AR events, the team expanded the study period to extend from November 2022 through April 2023.

### 2.3 Salinas River Watershed

The Salinas River Watershed (Figure 1) starts at an elevation of 4,000 ft. above sea level in the Santa Ynez mountains and drains around 4,600 square miles in Monterey and San Luis Obispo Counties (Monterey County Water Resources Agency, n.d.; Resource Conservation District of Monterey County, n.d.). The watershed encompasses 200,000 acres of irrigated farmland and is responsible for producing a significant portion of the United States lettuce, broccoli, artichokes, strawberries, and cauliflower (Resource Conservation District of Monterey County, n.d.). However, intensive farming has narrowed the riparian corridor, affecting wildlife, habitat, and water quality. The Salinas River and its valley have experienced flooding over the years due to the area's varied topography and rapid water movement. With more agricultural and urban expansion in flood-prone areas, the negative consequences of flooding have intensified. These floods along the Salinas River have resulted in considerable damage and economic hardships for the region (ICF, 2019).

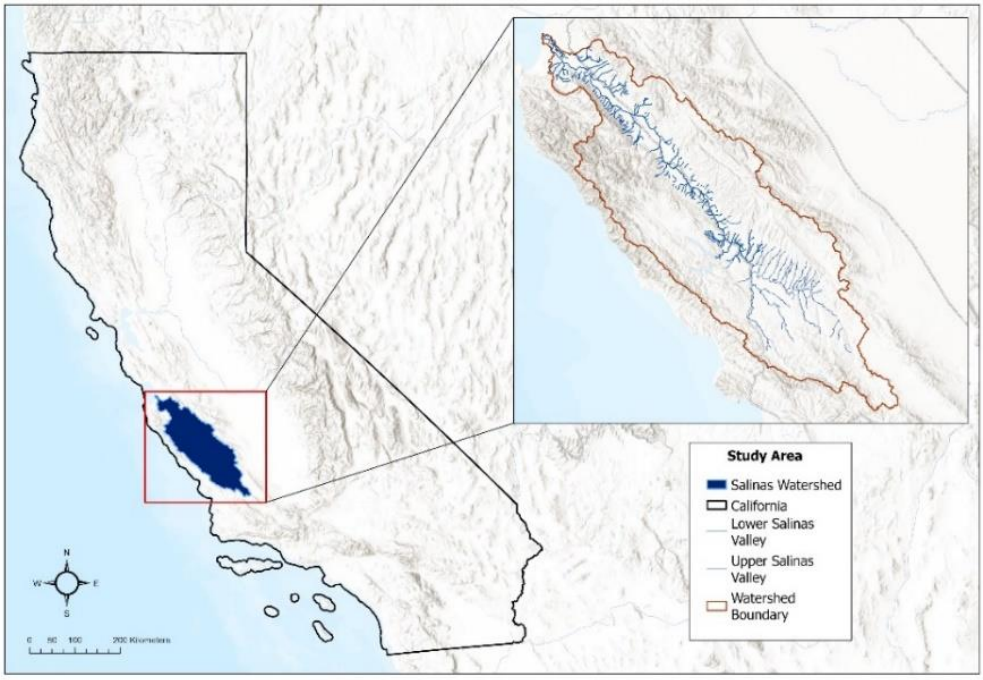


*Figure 1*. The Salinas River Watershed study area. [Basemap: California State Parks, Esri, TomTom, Garmin, FAO, NOAA, USGS, Bureau of Land Management EPA, NPS, USFWS, Esri, TomTom, Garmin, FAO, NOAA, USGS, EPA]

Based on the suggestions from the CA DWR, the team identified the cities of Bradley and San Miguel in the watershed as the vulnerable communities to focus on. The team also selected two AR events for deeper assessment, the events on January 14th, 2023, and March 10th, 2023.

### *2.3 Project Partners and Objectives*

Established in 1956 by the California State Legislature, the CA DWR protects, conserves, develops, and manages much of California's water supply. The CA DWR works on preventing and responding to floods, droughts, and other catastrophic events in the state. The ARs present a unique yet growing problem of causing billion-dollar flood events, significantly impacting agriculture, communities, and their livelihoods. The team collaborated with CA DWR to address data gaps in their flood risk assessment models for AR events by conducting a feasibility study on the use of Earth observations, including Global Precipitation Measurement (GPM)], Soil Moisture Active Passive (SMAP), and Sentinel-1, for monitoring ARs and AR-related flooding events.

## 3. Methodology

For the six distinct flooding events from December 2022 to March 2023, the team utilized different Earth observations and ancillary datasets. The GPM mission precipitation data and SMAP soil moisture measurements are the two NASA Earth observations used for this project. The team created comparative graphs with rain gauge data and quantitative precipitation values from Integrated Multi-Satellite Retrievals for GPM (IMERG) to assess the accuracy of the satellite-derived precipitation estimates, along with visualizing the variability of soil moisture throughout the events to assess hydrologic processes of water accumulation and drainage. Spatial plots helped visualize the hydrological changes across the days leading up to the AR events and in the days following the events. The team also generated bivariate plots for soil moisture and precipitation for the two events, to see if there were some emerging patterns. Additionally, since urban constructions can result in inaccurate soil moisture measurements, the team used the Arc-Malstrøm Blue Spot model to detect the accumulation of water in urban areas. For generating flood inundation maps, the team explored the

Moderate Resolution Imaging Spectroradiometer (MODIS) Near Real Time Global Flood Product in the NASA Land, Atmosphere Near real-time Capability for Earth observations (LANCE) through the Earth Observing System Data and Information System (EOSDIS) Worldview, but found that during the duration of our study, there was near constant cloud cover and hence there was no usable data. Therefore, the team used Sentinel-1 C-band Synthetic Aperture Radar (C-SAR) to create flood inundation maps, which were then used to verify the prediction of the Blue Spot Model. Lastly, the team used the Social Vulnerability Index (SVI) from the Center for Disease Control (CDC) to assess the vulnerability of communities due to floods using the Sentinel-1 imagery.

### *3.1 Data Acquisition*

The team acquired Earth observation data (Table 1) from the NASA EarthData web portal. The team utilized daily precipitation data (Late Run V06 and Final Run V07) from GPM IMERG. The Final Run data has a latency of approximately 3.5 months because it introduces precipitation gauge analysis and provides a much more accurate analysis for areas with gauge information. The Final Run (GPM IMERG-F) data is seen as a research-grade product (Huffman et al., 2023). To explore the operationalization of satellite data, the team used Late Run (GPM IMERG-L) data, which has a latency of about 14 hours. Since Late Run data has a shorter wait time, it is more useful for the CA DWR in their disaster response efforts (Huffman et al., 2023).

Soil moisture data was used from the SMAP Level 3 product data to identify the flood-prone areas in non-urban environments. The team used Landsat 8 Operational Land Imager (OLI) and Thermal Infrared Sensor (TIRS) as well as Landsat 9 OLI-2 and TIRS-2 surface reflectance datasets to classify the land cover characteristics of the study area before the 2022-2023 event. The team used Google Earth Engine to acquire Sentinel-1 C-SAR. The team acquired Vertical-Vertical (VV) and Vertical-Horizontal (VH) polarization for the analyses. Since Sentinel-1 C-SAR has an over-pass schedule of 6-12 days, there is a lag of 4 days from the date of AR events and the data is from the 18th of January 2023 and 14th of March 2023.

In addition, the team used several ancillary datasets to support the project's objectives (Table 1). The team obtained LiDAR data of the Salinas River Watershed from the United States Geological Survey (USGS) LiDAR Explorer to create a Digital Elevation Model (DEM) that identifies regions with higher waterlogging tendencies and other flood-contributing factors. The team acquired the SVI data from the CDC registry (Agency for Toxic Substances and Disease Registry, 2022) and used the census tract level of data to visualize the distribution of the vulnerability in the watershed.

Table 1
*Acquired Data and Data Sources*

| Platform | Data Source | Date(s) (mm/dd/yyyy) | Variable |
|---|---|---|---|
| SMAP (Enhanced L3 Radiometer Global and Polar Grid 9 km EASE-Grid Soil Moisture V005) | NASA Earthdata | 11/01/2022 - 04/30/2023 | Soil Moisture |
| GPM IMERG (V06 L3 1 day 0.1-degree x 0.1 degree) (GPM_3IMERGDL) | NASA Earthdata | 11/01/2022 - 04/30/2023 | Precipitation |
| GPM IMERG (V07 L3 1 day 0.1-degree x 0.1 degree) (GPM_3IMERGDF) | NASA Earthdata | 11/01/2022 - 04/30/2023 | Precipitation |
| Sentinel-1 C-SAR 5.405GHz (C band) GRD. 10 m | European Space Agency, using Google Earth Explorer | 11/01/2022 - 04/30/2023 | Water accumulation |

| | | | |
|---|---|---|---|
| Landsat 9 OLI-2/TIRS-2 (LaSRC v.1.5.0) | USGS via EarthExplorer | 11/29/2022 | Land Cover/ Land Use |
| Landsat 8 OLI/TIRS (LaSRC v.1.5.0) | USGS viaEarthExplorer | 11/28/2023 | Land Cover/ Land Use |
| LiDAR Point Cloud | USGS 3DEP LidarExplorer | NA | Elevation |
| Community Vulnerability Index | CDC | NA | Overall Ranking |

### *3.2 Data Preprocessing*

*3.2.1 SMAP:*

The team's processing for SMAP as well as GPM IMERG was performed using Python (v 3.9.18) in Spyder IDE and Python (v 3.11.5) in Visual Studio Code and Jupyter Notebooks. The various input files were in NetCDF format and read as xarray data frames. To focus the analysis on the relevant geographic region, the team clipped SMAP data to the spatial extent of the study area using ArcGIS Pro (v 3.2.1), ensuring that only the data within the designated study area was considered for further analysis. One of the primary challenges encountered in the preparation of SMAP data for analysis was dealing with data gaps resulting from orbital characteristics and cloud coverage. These gaps could significantly affect the accuracy of soil moisture estimates, particularly when generating spatial maps or temporal trends. To address this issue, the team developed a Python script to compute different rolling averages over specific time intervals, such as 3-day periods. Based on that, the program effectively handled missing data points, allowing for the generation of spatial plots with soil moisture values for most pixels within the study area.

*3.2.2 GPM IMERG:*

The CA DWR identified and verified seven rain gauge stations as the ones located in the study area, and the team used them for further analysis. To compare the difference in precipitation data captured by rain gauges and the satellites, the team focused on looking at values three days prior to and three days after each flooding event. Values from IMERG late run and final run were extracted for the nearest pixel to the rain gauge coordinates. These values were further used for evaluating the accuracy and performance of the GPM IMERG products to reproduce observed rainfall.

*3.2.3 Sentinel-1 C-SAR:*

To identify flood-prone areas, the team used Sentinel-1 C-SAR images to programmatically generate possible flood inundations. The images generated by Synthetic Aperture Radar (SAR) systems are subject to speckle noise, also known as salt and pepper distortion, due to the interference of the returning electromagnetic waves scattered from multiple surfaces. To combat this, the team used the speckle reduction function developed by Jong-Sen Lee, also known as the Lee function (Lee, 1980).

*3.2.4 Blue Spot Model:*

To assess urban flood susceptibility in an at-risk community, the team used the Blue Spot Model developed by Balstrøm, 2021. To use this model, the team first created a DEM of the case study city - Bradley, CA. After the team downloaded LiDAR point cloud data from the USGS 3DEP Lidar Explorer, the downloaded LAZ files were decompressed to LAS files using the uGet download manager. Then, in ArcGIS Pro 3.1.2, the team added these files to a new LAS Dataset before generating a raster DEM.

### *3.3 Data Analysis*

*3.3.1 GPM IMERG:*

Following the methods of Saouabe et al. (2020), the team used four metrics for assessing the accuracy and performance of the GPM IMERG-L and GPM IMERG-F products against the rain gauge observations: 1) Pearson's correlation coefficient was used to quantify the consistency between satellite-based precipitation data and rain gauge data, 2) mean error was used to evaluate the typical magnitude of error in satellite precipitation measurements, 3) root mean square error was used to express the average discrepancy between satellite-derived

data and observed precipitation value as derived from rain gauge data, and 4) relative bias (Bias) indicates the systematic deviation between the satellite products and the rain gauge observations. The equations for calculating the above statistical metrics are described in Equations A1 to A4.

The team also replicated the methodology used by Saouabe et al. (2020) to estimate the precipitation detection ability of the satellite product. Utilizing Table B1, the team calculated the probability of detection, which can be defined as the likelihood that a precipitation event will be correctly identified or detected by the satellite product. Probability of detection is calculated by dividing the number of events where precipitation was correctly observed by both the rain gauge and the satellite product by the total number of precipitation events as identified by rain gauges. The team also calculated the false alarm ratio, which can be defined as the fraction of precipitation events incorrectly identified when no precipitation was detected by the rain gauge station. It is determined by dividing the number of events where precipitation was observed only by the satellite by the total number of precipitation events as observed by satellite products.

*3.3.2 SMAP:*

After processing SMAP data to mitigate data gaps and spatial variability, the team analyzed the data to derive actionable insights. Within the study, the team generated plots for six flood events. Figure 2 shows plots produced for the December 27, 2022 AR. This figure shows a 3-day rolling average of soil moisture leading up to the flood and a 3-day rolling average during and following the flood events.

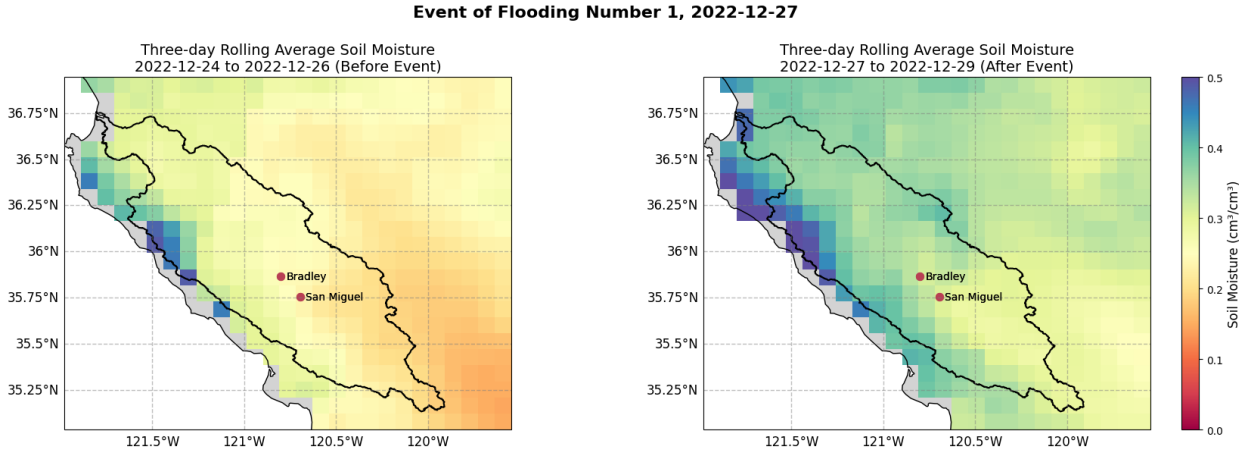


*Figure 2.* Soil moisture from the December 27th flood event

Drawing upon the methodology outlined by Rahman et al. (2019; Figure C1), the team utilized soil moisture saturation as an indicator of flood occurrence. The team calculated the difference between soil moisture values pre-flood and post-flood events with a 3-day rolling average to minimize data gaps. When the calculated difference exceeded 0.042 $cm^3/cm^3$ or the soil moisture surpassed a baseline porosity level of 0.45 $cm^3/cm^3$ for more than 72 hours, the team identified the geographical pixel as exhibiting saturated soil, indicative of a flood-prone area. The threshold of 0.042 $cm^3/cm^3$ was calculated by looking at the average increase of soil moisture in all events, while the 0.45 $cm^3/cm^3$ soil moisture baseline represents a value indicating high saturation given the scenario on hand.

Floods typically occur when soil is saturated past the maximum saturation threshold and significant water runoff ensues. Given that soil moisture levels are lower during dry conditions compared to wet conditions, an increase in soil moisture during saturation is expected. However, certain regions, such as lowlands and wetlands, may maintain full saturation throughout the year. Thus, while soil moisture typically rises after flooding, some areas experience perennial saturation. Hence, our analysis considered both the increase between pre-flood and post-flood conditions and the presence of consistently saturated soil.

*3.3.3 SMAP and GPM IMERG Integration:*

The team merged the outcomes of the SMAP and GPM IMERG analyses into a comprehensive bivariate plot to analyze their interrelated spatial patterns. This integration involved overlaying the GPM and SMAP images showcasing the highest levels of precipitation and soil moisture, respectively, to create a bivariate plot for visual comparison. For two AR events, the January 14th and March 10th, 2023 events, the team extracted pixels characterized by precipitation levels surpassing the 95th percentile threshold, indicative of extreme precipitation during this flooding event. Then the team selected pixels classified as saturated soil using the aforementioned Rahman et al. (2019) methodology. By isolating these pixels of interest, the team was able to delineate regions exhibiting the highest rates of rainfall alongside corresponding soil moisture saturation, thus facilitating an understanding of soil moisture and precipitation dynamics during these specific flooding events.

*3.3.4 Sentinel-1 C-SAR:*

The team adopted methodology from UN-Spider's Recommended Practice, "Flood Mapping and Damage Assessment Using Sentinel-1 C-SAR Data in Google Earth Engine" (United Nations Office for Outer Space Affairs, n.d.; Figure C2). Additionally, training from the NASA Applied Remote Sensing Training Program informed the utilization of SAR and the establishment of suitable thresholds. Flood detection thresholds vary depending on the geography and climatic conditions of the study area. For our study, the team employed a VH polarization and a threshold of -22 decibels (dB) to indicate water presence and devised a change detection technique, identifying pixels surpassing the water threshold. Utilizing images captured before and after specific dates (i.e., August 2022 as the "before" image and 18th January and 14th March 2023 as the "after" images), flood inundations were determined by pixels exhibiting more than -22dB before the event (indicating non-water) and less than -22dB after the event (indicating water presence thereafter). Figure 3 illustrates potential flood inundations resulting from the two events.

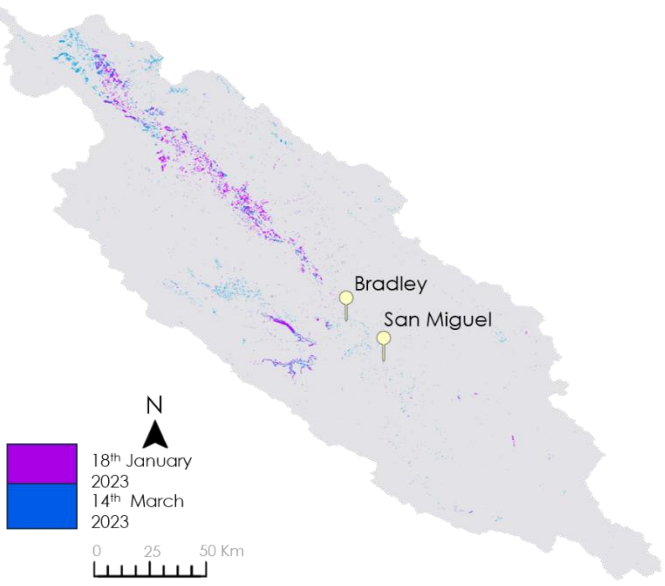


*Figure 3.* Possible flood inundations from January 18th and March 14th.

*3.3.5 Landsat 8 & 9:*

To classify the land use and land cover characteristics of the Salinas River Watershed before the 2022 AR event, the team extracted two Landsat 8 OLI/TIRS and Landsat 9 OLI-2/TIRS-2 imagery datasets from USGS's Earth Explorer. The Surface Reflectance datasets for each raster were then added to a mosaic dataset in ArcGIS Pro, which was then selected as an input for the Classify Pixels Using Deep Learning tool. Then, using the

Land Cover Classification model created by Esri, the team processed both images before clipping them to the relevant study area.

*3.3.6 Blue Spot Model:*
After the team created a 1-meter DEM of Bradley, California, the DEM was then hydrologically conditioned using ArcGIS Pro. The conditioned DEM was then used as the primary input for the Blue Spot model workflow. Once the model was complete, the team then compared its outputs to the outputs gathered from Sentinel-1 C-SAR imagery.

# 4. Results & Discussion

## *4.1 Analysis of Results*

*4.1.1 SMAP:*
To analyze SMAP data, the team produced line plots and spatial diagrams instrumental in evaluating soil moisture dynamics during flooding occurrences. The team also created a map of Boolean values to show the distribution of highly saturated pixels classified using the methodology modified from Rahman et al. (2019). The maps identify pixels exhibiting high saturation levels, which are indicative of heightened susceptibility to flooding compared to drier counterparts.

Line plots are insightful tools for evaluating soil moisture trends across designated study intervals. The illustration below focuses on the geographic pixel nearest to Bradley, California. The plot in Figure 4 visualizes both soil moisture variation over time and underlying trends, including recurrent dry or wet spells. Abrupt deviations in the line signal correspond to shifts in moisture levels; these deviations often coincide with periods of intense rainfall, denoted by the dashed red lines. Such insights prove valuable for agricultural strategies, irrigation planning, and environmental monitoring.

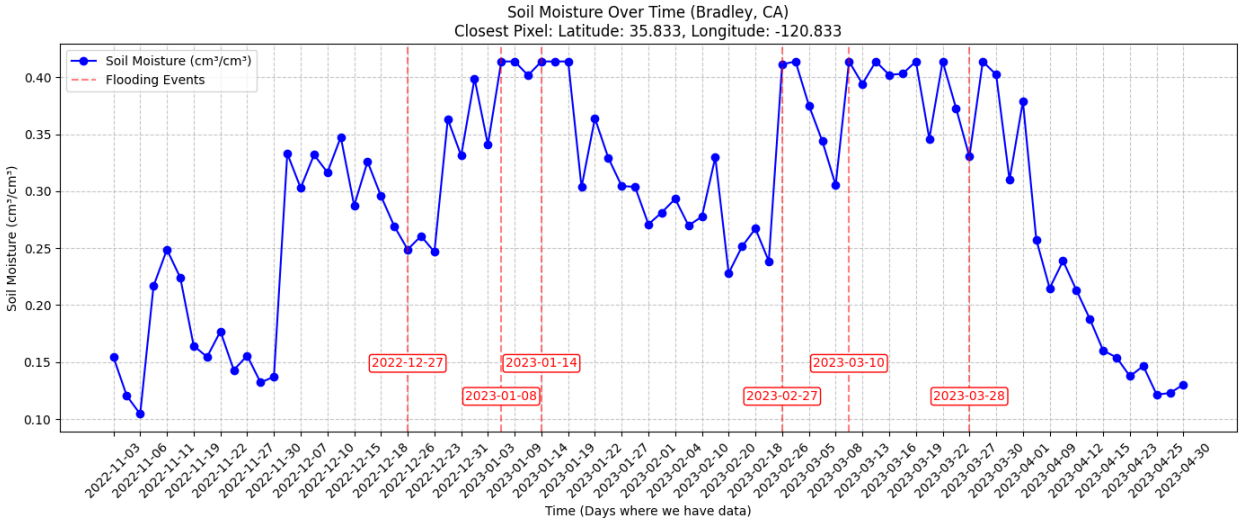


*Figure 4.* Soil moisture changes between November 2022 and April 2023 in Bradley, CA

The insights gained from Boolean maps regarding flood-prone areas (Figure 5), characterized by highly saturated soil, hold value for various purposes. They can be leveraged by the CA DWR for tasks ranging from risk assessment to emergency response and post-flood analysis. By integrating this information into decision-making processes, stakeholders can enhance preparedness, response efficiency, and overall resilience in the face of flood events.

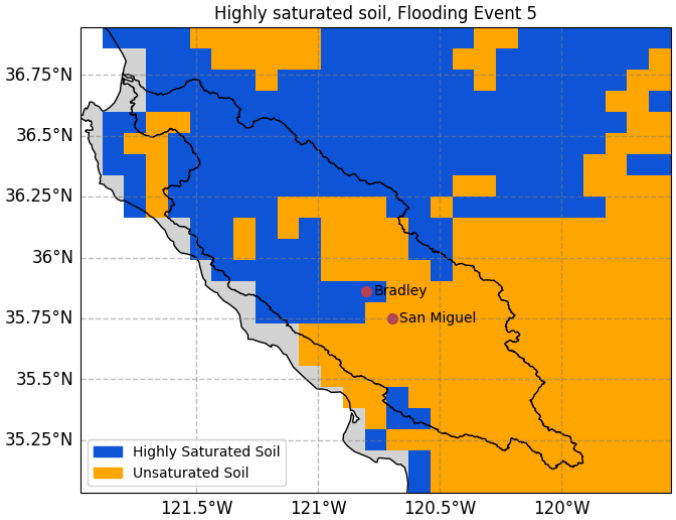


*Figure 5.* Locations of highly saturated soil following the March 10th flooding event

*4.1.2 GPM IMERG*:
After comparing the satellite precipitation products with rain gauge station data, the team found that NASA's GPM IMERG-F rain measurements have an average relative error of 33% compared to on-the-ground rain gauge data. In other words, on average, GPM IMERG-F underestimates precipitation by about 9mm compared to the rain gauge data. Meanwhile, GPM IMERG-L underestimates precipitation by an average of about 10mm. The results (Table B2) reveal a negative relative bias, indicating that satellite precipitation products tend to underestimate precipitation values compared to those measured by rain gauges. Similarly, a visual comparison of different rain gauge stations during various flooding events revealed a consistent pattern of underestimation (Table B1).

The underestimation of precipitation by satellite products may stem from several factors, including beam filling effects and inaccuracies due to orographic enhancement are notable. Satellite rainfall retrieval algorithms, which rely on a physical approach, often assume that the rainfall rate within each satellite beam is uniform. However, rainfall distribution is not always uniform across these beams, leading to discrepancies between satellite-derived precipitation rates and in situ measurements, a discrepancy known as the beamfilling error (Kummerow, 1998). Additionally, inaccuracies can also arise from orographic enhancement, a phenomenon where air masses lifted by terrain condense and form clouds, resulting in increased rainfall with altitude. This process may contribute to the challenges in underestimating rainfall by GPM IMERG (Rojas et al., 2021).

The bivariate analysis shown in Figure 6 uses both GPM IMERG and SMAP data to highlight areas classified as potential saturation zones. The plots identify overlapping pixels that are classified as both "saturated" according to the Rahman et al. (2019) methodology and surpass the 95th percentile precipitation threshold, providing valuable insights into the concurrent impact of intense precipitation and soil moisture levels. Through this integration of SMAP and GPM IMERG data, the team aims to offer a nuanced perspective on the relationship between precipitation patterns and soil moisture dynamics during notable flooding events, ultimately contributing to enhanced flood monitoring and analysis methodologies.

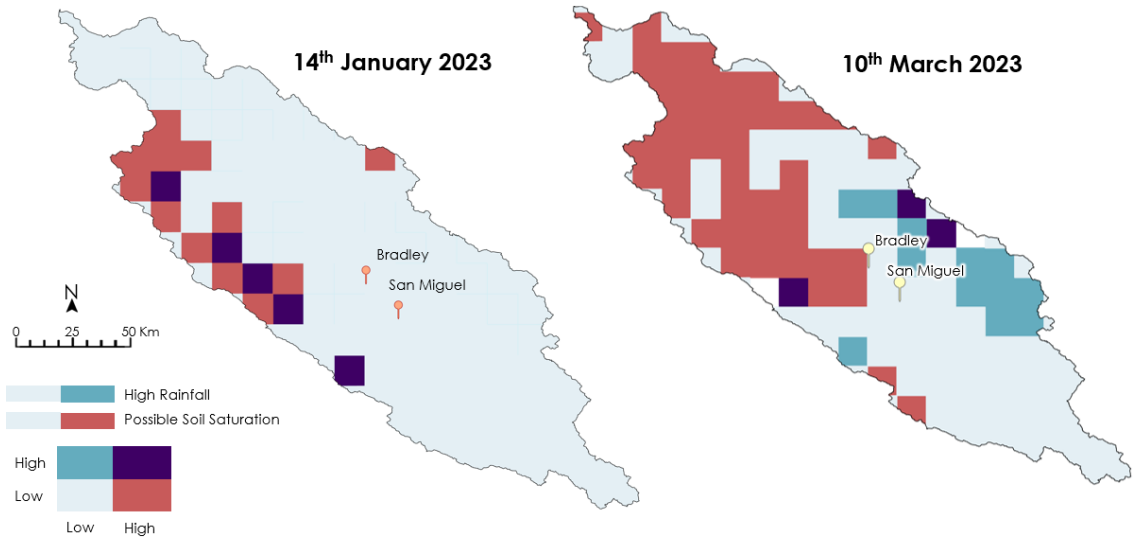


*Figure 6*. Potential flooding at the neighborhood scale

*4.1.3 Sentinel-1 C-SAR*:

For our case study of January 14th and March 10th, the imagery is not available until January 18th and March 14th, respectively. In terms of actual patterns, some clusters are seen along the river and other water bodies in the watershed, which is quite accurate. Figure 7 shows some overlapping clusters of flooded pixels on the left side. On the right side, the team mapped the same inundations and added the river and two lakes in the base layer.

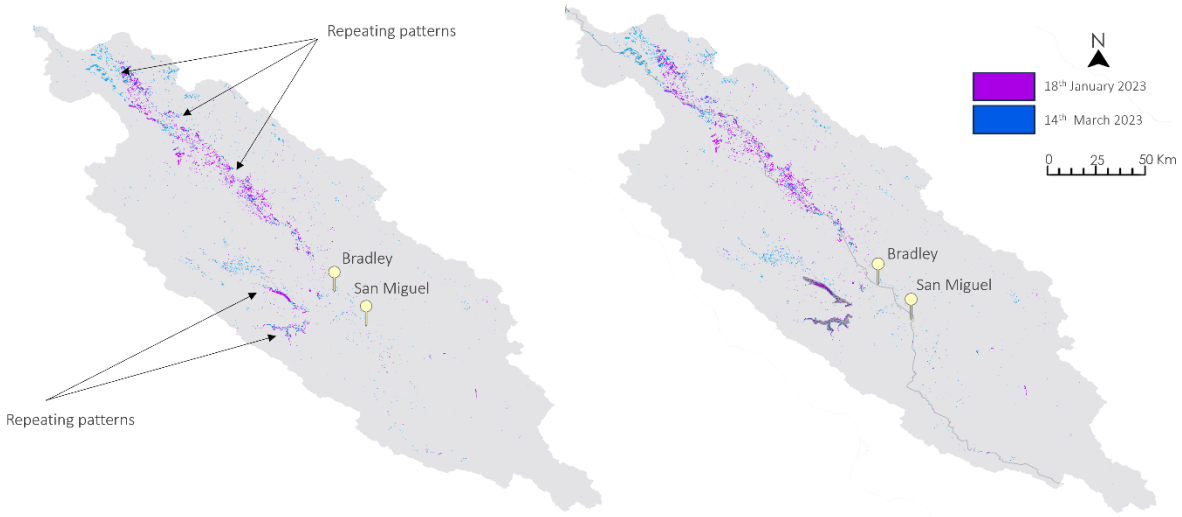


*Figure 7*. Potential flooding at the neighborhood scale.

*4.1.4 Social Vulnerability*

The distribution of social vulnerability by census tracts (Figure 8) are taken from the CDC (Agency for Toxic Substances and Disease Registry, 2022). The SVI is a cumulative index, which accounts for socioeconomic status, household characteristics, racial and ethnic minority status, and housing type and transportation. When the possible flood inundations generated by Sentinel-1 C-SAR are overlayed on the SVI in Figure 8, an

interesting pattern can be seen. The brighter spots, denoting higher concentration of possible flood inundations, lie within census tracts above the 50% threshold of social vulnerability almost 80% of the time.

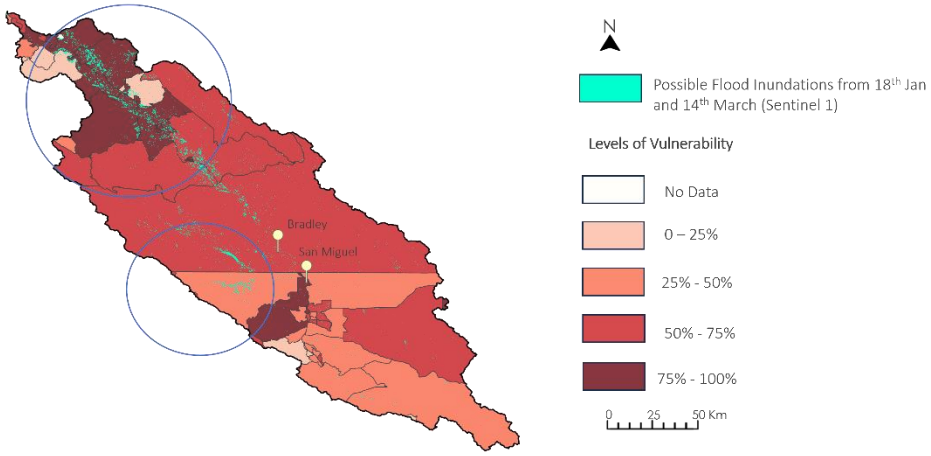


*Figure 8*. Potential flooding at the neighborhood scale.

*4.1.5 Land Use/Land Cover:*

The Land Use/Land Cover classification (Figure 9) showed that most of the Salinas Watershed as covered in shrubland and forests as of November 2022. Along the Salinas River, the northern portion of the valley was composed of cultivated cropland and urban areas. For Bradley, much of the small town was classified as low-to-moderately developed and the surrounding locations were a mixture of wetlands, agricultural lands, and shrublands. Because these varying characteristics affect surface infiltration, runoff retention, and overall flooding, CA DWR may utilize this information to establish specialized flood management systems for specific locations within the valley.

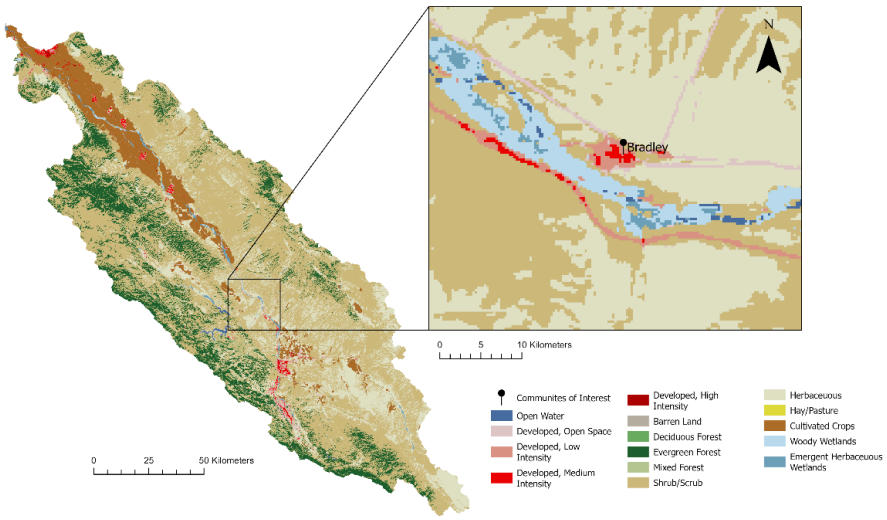


*Figure 9*. The Salinas River Watershed land cover classification.

*4.1.6 Blue Spot*:

The outputs from the Blue Spot model highlighted locations where water could accumulate during a heavy rainfall event, both in and around the city of Bradley. As seen in Figure 10, areas located at lower elevations,

areas near the Salinas River, major roadways, and areas along the Southern Pacific Railroad were identified as sites of possible pluvial flooding. Additionally, a comparison with Sentinel-1 C-SAR imagery showed that three locations near predicted inundation sites were repeatedly flooded during the floods on January 18th and March 14th (Figure 11). While further study is needed to verify the accuracy of the model, CA DWR could use this model for flood risk prediction in urban settings.

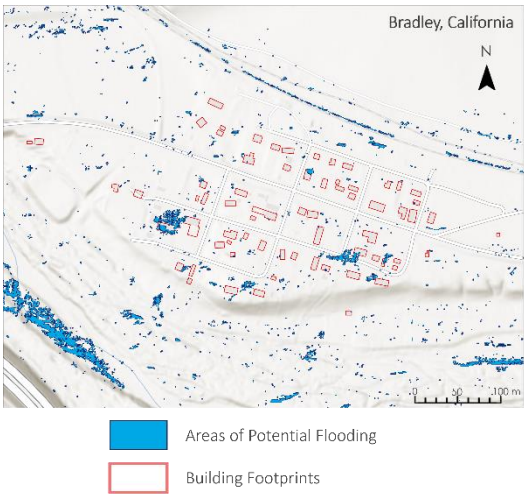


*Figure 10.* Potential flooding at the neighborhood scale.

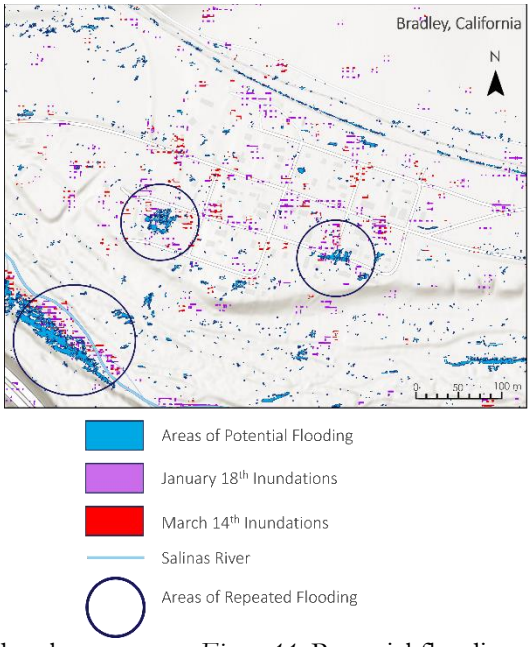


*Figure 11.* Potential flooding comparison.

### *4.2 Feasibility for Partner Use*

*4.2.1 GPM-IMERG:*

The team's analysis of the GPM-IMERG data provides a quantitative estimate of the measurement errors in satellite-derived precipitation compared to rain gauge data. The methodology can be replicated to further evaluate accuracy over a longer time series and incorporate more rain gauge stations. These estimates allow partners to determine if the errors fall within acceptable limits for using satellite data to obtain precipitation estimates in areas with few rain gauge stations. They can then assess the usability of satellite precipitation products in disaster response.

*4.2.2 SMAP:*

Regarding SMAP analysis, it is important to note certain limitations. Unlike the GPM IMERG methodology, the team faced challenges in verifying the accuracy of satellite-derived soil moisture values and comparing them with in situ ground-based approaches within the project timeframe. Additionally, there was a lack of comparison between saturated (and hence flood-prone) areas and actual flooding maps due to the absence of in situ flood maps matching our spatial resolution of 9-km.

Another limitation lies in the method used to calculate the threshold of 0.042 $cm^3/cm^3$ for identifying highly saturated areas within the SMAP analysis. During the project, this value was calculated by examining all data points (geographic pixels) for each pre- and post-phase of six flooding events and determining the average of the absolute distances between pre- and post-flooding. Consequently, many geographic pixels in the plot of the first flooding event on the 27th of December 2022 were marked as "saturated and therefore prone to flooding" due to significant increases in soil moisture. Therefore, this approach may not accurately represent actual flood-prone areas because the soil was generally much drier before the very first flood event compared to subsequent events.

*4.2.3 Sentinel-1 C-SAR:*

The ability to analyze past floods and AR events helps us inform future climate action. Looking at historical flood events helps to establish patterns. For this purpose, Sentinel-1 C-SAR is an attractive Earth observation data product due to the use of SAR. SAR is not affected due to clouds or tree canopy and is extremely useful for identifying flooded areas and will be imperative in establishing flood behaviors during ARs. It helps fill the gaps that satellites like MODIS and Landsat have. Unfortunately, due to a repeat cycle of 6 to 12 days, Sentinel-1 C-SAR data misses the AR events by a few days during the study period and the flood maps generated through it represent the possible floods on the day when it passed. However, the user guide for Sentinel mentions a Near Real-Time emergency response within 1 hour of the emergency and 3 hours for Near Real-Time priority areas. In case of emergencies, the CA DWR may still explore the use of Sentinel-1 C-SAR data.

SAR, however, has limitations in terms of accuracy. In urban areas, microwave radiation emitted by SAR instruments can detect shadows near buildings, which might be misidentified as false positives for flood risk. Similarly, wet roads or airstrips may be misinterpreted as false positives due to their flat surfaces, which may appear as standing water.

*4.2.4 Blue Spot Model*

The Blue Spot model is an urban flood risk model that the CA DWR can access easily through Python packages and ArcGIS Pro. The model gives reference to areas with the potential for pluvial flooding based on elevation, buildings, and flow lines. However, it is important to note that the model does not account for changes in weather conditions and actual flooding locations are not limited to predicted spillover sites. Additionally, the model does not account for man-made drainage systems, which can alter the natural flow pattern of water and reduce the accuracy of flood predictions. Lastly, the spatial resolution of the model may not accurately represent small-scale features like buildings, which can lead to inaccurate predicted flooding extents.

### *4.3 Future Recommendations*

*4.4.1 SMAP:*

To address the limitations highlighted in Section 4.2, the soil moisture values derived from SMAP data and the saturation map produced should be validated. This validation should be conducted using ground-truth measurements of soil moisture obtained through in situ methods, as well as real-time flood maps.

A promising approach for this validation process involves utilizing a downscaled version of SMAP data, developed by Fang et al. (2022) which offers a spatial resolution of 1-km. By leveraging this downscaled dataset, which aligns with the spatial resolution of the generated saturation map, a thorough comparison can be made. By corroborating SMAP-derived soil moisture values and the saturation map against ground-truth measurements and flood maps, the reliability and accuracy of our analysis is enhanced. This validation step will not only help identify any discrepancies or errors but also strengthen the overall validity of the findings presented in earlier chapters.

As a prospective strategy to address the issue of biased saturation maps stemming from the averaged increase of soil moisture, a refined approach could involve calculating the threshold for each flooding event rather than aggregating data over a specified period containing multiple events. This tailored methodology holds promise in enhancing stability, particularly in mitigating the influence of outliers, thereby improving the robustness of the SMAP analysis.

*4.4.2 GPM IMERG:*

The team investigated the performance of GPM IMERG-L and GPM IMERG-F and their potential use in disaster response for the CA DWR. However, further research could evaluate the accuracy and usability of using GPM IMERG Early (GPM IMERG-E) run data. GPM IMERG-E has a latency of 4 hours (Huffman et al., 2023), making it potentially more useful for immediate disaster response.

*4.4.3 Sentinel-1 C-SAR:*

In the future, Sentinel-1 data should be used to plot all possible flood inundations for the entire study period and check for patterns. In order to validate the Sentinel-1 maps, the coordinates of potential flood inundations identified using Sentinel-1 should be checked against on-the-ground reports of flooding in the Salinas River Watershed. Future work should also include a thorough statistical analysis of past co-occurrence and the probability of future co-occurrence of flooding events within census tracts of relatively high scores on the SVI.

## 5. Conclusions

The purpose of this study was to identify the feasibility of using NASA Earth observations to better assess flooding caused by ARs in Central California. The team found that SMAP served as a valuable flooding indicator that could be visualized through graphical representations like lines or spatial plots. But, to accurately identify flood-prone regions, spatial resolution downscaling, and verification through in situ flood maps are necessary. In exploring the use of precipitation measurements from satellite-based products to fill in data gaps in areas with limited in situ measurements, the team found that GPM IMERG consistently underestimates rainfall measurements with an average relative error of 33-52%, which aligns with other scientific research (Graves 1993; Chiu et al., 1990). The team identified that the CA DWR could benefit from SAR imagery in cases of pluvial flooding and ARs due to its cloud penetration capacities. In terms of flood risk modeling, the Blue Spot Model shows potential for pinpointing flooding at a neighborhood scale. However, it may not be as useful in less populated or rural areas. Furthermore, initial findings suggest a positive correlation between flooding and vulnerability, nevertheless, further investigation is needed for confirmation of these insights. Overall, though the team sees potential in using these datasets to assess flooding, further verification is needed to determine accuracy.

## 6. Acknowledgements

The team wants to acknowledge our project partner California Department of Water Resources (CA DWR), for entrusting us with this project. The team is incredibly grateful to Dr. MD Haque (CA DWR), Dr. Michael Anderson (CA DWR), Weihua Li (CA DWR), and Essayas Ayana (CA DWR) for their technical guidance and constructive feedback on our methodology, results, and findings. Our special thanks go to our science advisors, Dr. Xia Cai (NASA Langley Research Center), Dr. Kenton Ross (NASA Langley Research Center), and Dr. Venkataraman Lakshmi (University of Virginia), whose expertise and feedback helped shape and implement our project. The team is also grateful to Benjamin Goffin (University of Virginia), Aashutosh Aryal (University of Virginia) as well as Dr. Bin Fang (University of Virginia) who ensured a seamless collaboration between NASA DEVELOP and the UVA Pop-Up location. Lastly, the team would like to extend its sincere gratitude to our Lead, Isabel Lubitz (Maryland – Goddard), whose constant and endearing support towards our team helped make our project successful.

This material contains modified Copernicus Sentinel data (2023), processed by ESA.

Any opinions, findings, and conclusions or recommendations expressed in this material are those of the author(s) and do not necessarily reflect the views of the National Aeronautics and Space Administration.

This material is based upon work supported by NASA through contract 80LARC23FA024.

## 7. Glossary

**ArcGIS Pro:** A geographic information system (GIS) software used for creating, managing, analyzing, and
**Bivariate plot:** A graphical representation displaying the relationship between two variables.
**Boolean spatial plot:** A graphical representation where data values are either true or false, typically used to visualize binary relationships.
**CA DWR:** California Department of Water Resources: A state agency responsible for managing and protecting California's water resources.
**C-band:** A frequency range commonly used in radar systems, including the Sentinel-1 SAR, known for its ability to penetrate vegetation and provide detailed imaging of the Earth's surface.

**Change Detection Technique:** Methodology employed to identify pixels surpassing the water threshold, indicating flood inundations.
**Digital Elevation Model:** A digital representation of the Earth's surface topography.
**Extreme Precipitation:** Intense or heavy rainfall exceeding typical levels.
**Flood Monitoring:** Systematic observation and analysis of water levels and related factors to predict and respond to flooding events.
**Google Earth Engine:** A cloud-based platform developed by Google for geospatial data analysis and visualization.
**GPM IMERG:** Global Precipitation Measurement Integrated Multi-Satellite Retrievals: A satellite-based system that provides near-real-time precipitation data.
**Inundated areas:** Regions flooded with water.
**Perennial saturation:** Continual saturation of soil with water throughout the year.
**Polarization:** The orientation of the electric field in a radar wave. SAR systems can operate in different polarization modes (e.g., HH, VV, HV) to capture different scattering characteristics of the Earth's surface.
**Porosity:** The volume of void space in soil or rock.
**Python script:** A program written in the Python programming language used to automate tasks or manipulate data.
**Rolling averages:** A statistical technique used to analyze trends by calculating the average of a subset of consecutive data points over a defined time period.
**Saturation zones:** Areas where soil moisture levels have reached full capacity.
**Sentinel-1:** A European Space Agency (ESA) satellite mission that provides Synthetic Aperture Radar (SAR) data for various applications, including land and ocean monitoring.
**SMAP:** Soil Moisture Active Passive: A satellite mission by NASA aimed at measuring soil moisture and freeze/thaw state globally using microwave radiometers and radar.
**Social Vulnerability Index (SVI):** Cumulative index accounting for socioeconomic status, household characteristics, racial and ethnic minority status, housing type, and transportation, used to assess social vulnerability to natural disasters.
**Speckle:** Random noise or interference in SAR images caused by the coherent nature of radar waves. Speckle can reduce image quality and complicate interpretation but can be mitigated through filtering techniques.
**Synthetic Aperture Radar (SAR):** A remote sensing technology that uses radar to create high-resolution images of the Earth's surface by transmitting and receiving microwave signals.
**VH Polarization:** Vertical-horizontal polarization mode used in SAR imaging.

## 8. References


Agency for Toxic Substances and Disease Registry. (2022). CDC SVI Documentation 2020. https://www.atsdr.cdc.gov/placeandhealth/svi/documentation/SVI_documentation_2020.html

Balstrøm, T. (2021). *Model bluespots to map flood risk: Explore bluespots in a drainage basin north of Copenhagen, where homes and critical infrastructure located in landscape sinks are filled during rainstorms*. Esri. https://learn.arcgis.com/en/projects/model-bluespots-to-map-flood-risk/

Chiu, L. S., North, G. R., Short, D. A., & McConnell, A. (1990). Rain estimation from satellites: Effect of finite field of view. Journal of Geophysical Research: *Atmospheres, 95(*D3), 2177–2185. https://doi.org/10.1029/JD095iD03p02177

Fang, B., Lakshmi, V., Cosh, M., Liu, P.-W., Bindlish, R., & Jackson, T. J. (2022). A global 1-km downscaled SMAP soil moisture product based on thermal inertia theory. *Vadose Zone Journal, 21*(2), e20182. https://doi.org/10.1002/vzj2.20182

Friedrich, H.K., Tellman, B., Sullivan, J.A., Saunders, A., Zuniga-Teran, A.A., Bakkensen, L.A., Cawley, M., Dolk, M., Emberson, R.A., Forrest, S.A., Gupta, N., Gyawali, N., Hall, C.A., Kettner, A. J., Lozano, J.L.S., & Bola, G.B. (2024). Earth observation to address Inequalities in Post-Flood Recovery. *Earth's Future, 12*(2), e202EF003606. https://doi.org/10.1029/2023EF003606

Gimeno, L., Nieto, R., Vázquez, M., & Lavers, D. (2014). Atmospheric rivers: A mini-review. *Frontiers in Earth Science*, *2*. https://www.frontiersin.org/articles/10.3389/feart.2014.00002

Graves, C. E. (1993). A Model for the Beam-filling Effect Associated with the Microwave Retrieval of Rain. *Journal of Atmospheric and Oceanic Technology, 10*(1), 5–14. https://doi.org/10.1175/1520-0426(1993)010<0005:AMFTBF>2.0.CO;2

Guan, B., Molotch, N. P., Waliser, D. E., Fetzer, E. J., & Neiman, P. J. (2010). Extreme snowfall events linked to atmospheric rivers and surface air temperature via satellite measurements. *Geophysical Research Letters*, *37*(20). https://doi.org/10.1029/2010GL044696

Huffman, G. J., Bolvin, D. T., Joyce, R., Kelley, O. A., Nelkin, E. J., Tan, J., Watters, D. C., & West, B. J. (2023). Integrated Multi-satellitE Retrievals for GPM (IMERG) Technical Documentation. https://gpm.nasa.gov/sites/default/files/2023-07/IMERG_TechnicalDocumentation_final_230713.pdf

Inner City Fund International. (2019). *Salinas River Long-Term Management Plan* (p. 274). ICF. https://www.salinasrivermanagementprogram.org/documents/ltmp_doc/salinasriver_ltmp_stacked.pdf

Kummerow, C. (1998). Beamfilling Errors in Passive Microwave Rainfall Retrievals. *Journal of Applied Meteorology and Climatology, 37*(4), 356–370. https://doi.org/10.1175/1520-0450(1998)037<0356:BEIPMR>2.0.CO;2

Lee, J.-S. (1980). Digital Image Enhancement and Noise Filtering by Use of Local Statistics. *IEEE Transactions on Pattern Analysis and Machine Intelligence, PAMI-2*(2), 165–168. https://doi.org/10.1109/TPAMI.1980.4766994

Monterey County Water Resources Agency. (n.d.). *Major Flood Hazards*. Monterey County Water Resources Agency. https://www.co.monterey.ca.us/government/government-links/water-resources-agency/programs/floodplain-management/major-flood-hazards

Neiman, P. J., Ralph, F. M., Wick, G. A., Lundquist, J. D., & Dettinger, M. D. (2008). Meteorological Characteristics and Overland Precipitation Impacts of Atmospheric Rivers Affecting the West Coast of North America Based on Eight Years of SSM/I Satellite Observations. *Journal of Hydrometeorology*, *9*(1), 22–47. https://doi.org/10.1175/2007JHM855.1

NOAA National Centers for Environmental Information. (2024) *U.S. Billion-Dollar Weather and Climate Disasters*. https://www.ncei.noaa.gov/access/billions/

Rahman, M. S., Di, L., Yu, E., Lin, L., Zhang, C., & Tang, J. (2019). Rapid Flood Progress Monitoring in Cropland with NASA SMAP. *Remote Sensing, 11*(2), 191. https://doi.org/10.3390/rs11020191

Ralph, F. M., Neiman, P. J., Wick, G. A., Gutman, S. I., Dettinger, M. D., Cayan, D. R., & White, A. B. (2006). Flooding on California's Russian River: Role of atmospheric rivers. *Geophysical Research Letters*, *33*(13). https://doi.org/10.1029/2006GL026689

Resource Conservation District of Monterey County. (n.d.). *Salinas River Watershed*. Resource Conservation District of Monterey County. https://www.rcdmonterey.org/salinas-river

Rojas, Y., Minder, J.R., Campbell, L. S., Massmann, A., & Garreaud, R. (2021). Assessment of GPM IMERG Satellite precipitation estimation and its dependence on microphysical rain regimes over the mountains of south-central Chile. *Atmospheric Research, 253*, 105454. https://doi.org/10.1016/j.atmosres.2021.105454

Saouabe, T., El Khalki, E. M., Saidi, M. E. M., Najmi, A., Hadri, A., Rachidi, S., Jadoud, M., & Tramblay, Y. (2020). Evaluation of the GPM-IMERG Precipitation Product for Flood Modeling in a Semi-Arid Mountainous Basin in Morocco. *Water, 12*(9), 2516. https://doi.org/10.3390/w12092516

United Nations Office for Outer Space Affairs. (n.d.). *Step-by-Step: Recommended Practice: Flood Mapping and Damage Assessment Using Sentinel-1 SAR Data in Google Earth Engine*. UN-SPIDER Knowledge Portal. https://www.un-spider.org/advisory-support/recommended-practices/recommended-practice-google-earth-engine-flood-mapping/step-by-step

Wen, Y., Behrangi, A., Chen, H., & Lambrigtsen, B. (2018). How well were the early 2017 California Atmospheric River precipitation events captured by satellite products and ground-based radars? *Quarterly Journal of the Royal Meteorological Society*, *144*(S1), 344–359. https://doi.org/10.1002/qj.3253

# 9. Appendices

**Appendix A**

Equation A1: $CC = \frac{\sum_{i=1}^{n}(G_i-\bar{G})(S_i-\bar{S})}{\sqrt{\sum_{i=1}^{n}(G_i-\bar{G})^2}\times\sqrt{\sum_{i=1}^{n}(S_i-\bar{S})^2}}$

Equation A2: $ME = \frac{\sum_{i=1}^{n}(S_i-G_i)}{n}$

Equation A3: $RMSE = \sqrt{\frac{\sum_{i=1}^{n}(S_i-G_i)^2}{n}}$

Equation A4: Relative Bias $= \frac{\sum_{i=1}^{n}(S_i-G_i)}{\sum_{i=1}^{n}G_i}\times 100$

*(Equations from Saouabe et al., 2020)*

Where n represents the sample size, $S_i$ is the satellite precipitation estimate, $G_i$ is the observed precipitation from the rain gauge, S is the mean satellite precipitation estimate, and G is the mean rain gauge precipitation observation (Saouabe et al., 2020).

## Appendix B

Table B1.
*Contingency table for calculation of Probability of detection and False Alarm Ratio*

| | | **Observation** | | |
|---|---|---|---|---|
| | | **Yes** | **No** | |
| GPM IMERG | **Yes** | A: Hits (observed by IMERG and Rain Gauge) | B: False (observed only by satellite) | A+B: Observed by Satellite |
| | **No** | C: Misses (observed only by rain gauge) | D: Rejection (observed by neither) | C+D: Not observed by Satellite |
| | | A+C: Observed by rain gauges | B+D: Not observed by rain gauges | N: Total of events |

*(table taken from Saouabe et al., 2020)*

Probability of detection (POD) = A/(A+C), False Alarm ratio (FAR) = B/(A+B)

Table B2.
*GPM IMERG – Statistical Analysis*

| Sl No. | Rain Gauge | Satellite Product | CC | Relative Bias (%) | ME (mm) | RMSE (mm) | POD | FAR |
|---|---|---|---|---|---|---|---|---|
| 1 | ARY | GPM IMERG -F | 0.843 | -48 | 9.9 | 17.6 | 0.931 | 0.069 |
| | | GPM IMERG -L | 0.872 | -52.5 | 9.7 | 18.4 | 0.965 | 0.152 |
| 2 | PKF | GPM IMERG -F | 0.834 | -8.5 | 4.5 | 8.7 | 0.857 | 0.2 |
| | | GPM IMERG -L | 0.813 | -44.2 | 5.3 | 9.8 | 0.929 | 0.212 |
| 3 | PSB | GPM IMERG -F | 0.913 | -5.9 | 2.7 | 5.1 | 0.913 | 0.25 |
| | | GPM IMERG -L | 0.822 | -29.3 | 3.7 | 7.1 | 0.869 | 0.31 |
| 4 | PAS | GPM IMERG -F | 0.834 | -20.6 | 5.5 | 10.4 | 0.852 | 0.179 |
| | | GPM IMERG -L | 0.741 | -46.9 | 6.3 | 13.2 | 0.889 | 0.172 |
| 5 | BLM | GPM IMERG -F | 0.789 | -54.4 | 14 | 31.5 | 0.833 | 0.2 |
| | | GPM IMERG -L | 0.851 | -72 | 15.5 | 34.8 | 0.917 | 0.29 |
| 6 | SMB | GPM IMERG -F | 0.751 | -60.9 | 19.6 | 40.1 | 0.957 | 0.214 |
| | | GPM IMERG -L | 0.728 | -69.2 | 20.2 | 42.8 | 0.957 | 0.29 |

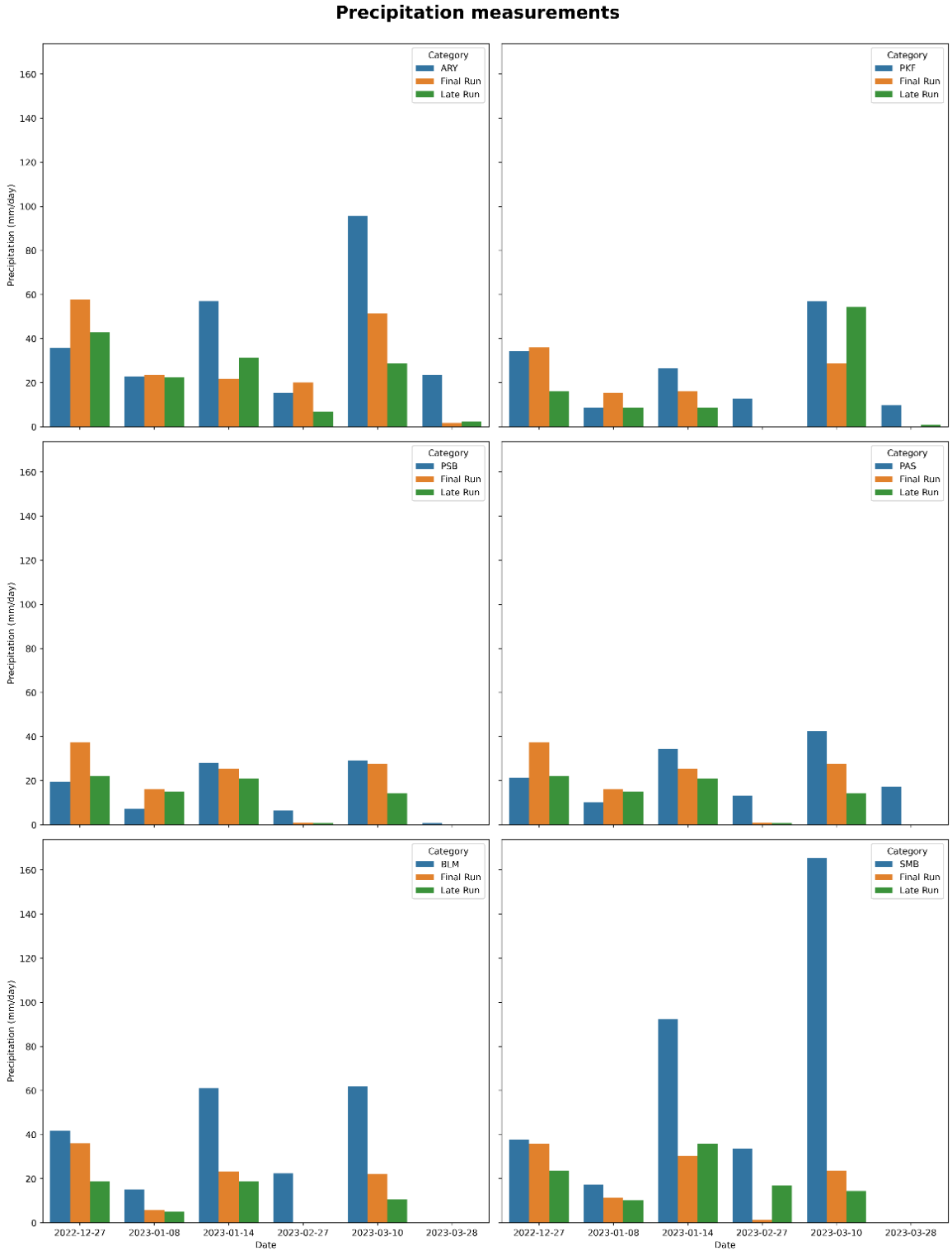


*Figure B1.* Comparison of precipitation measurement by different rain gauge stations and satellite precipitation products on six flooding dates

## Appendix C

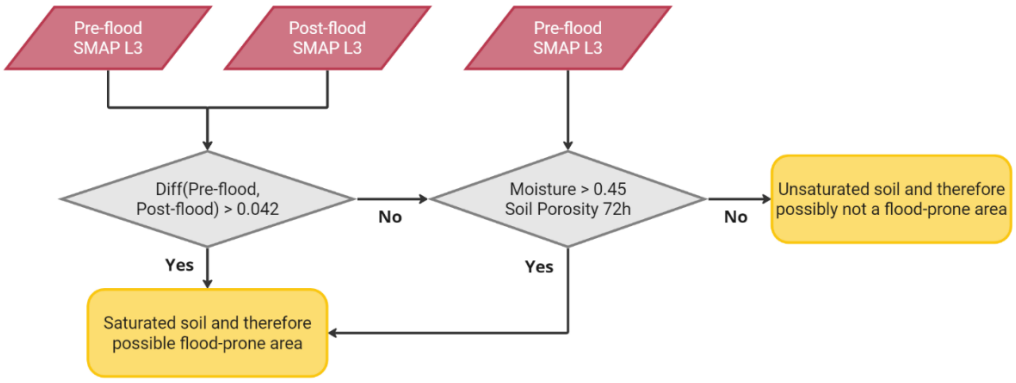


*Figure C1.* Flow diagram describing the approach for analyzing SMAP data.

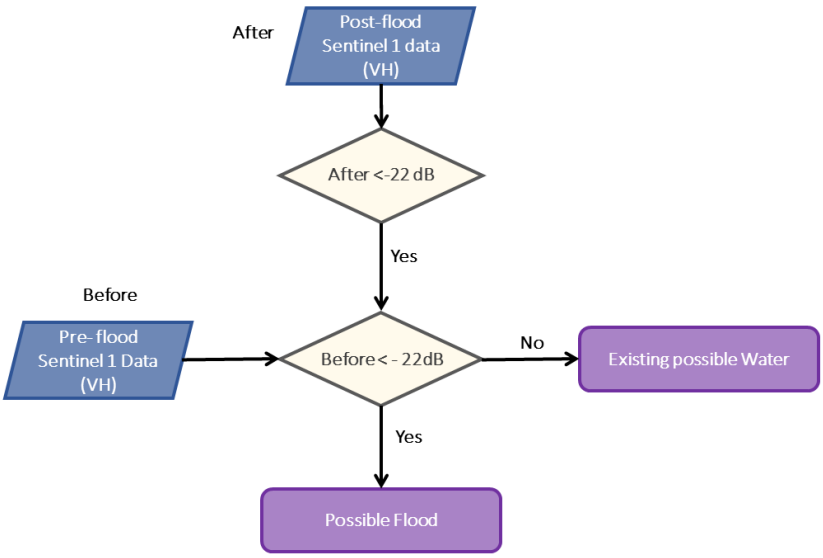


*Figure C2.* Sentinel-1 flood inundations methodology. Adapted from UN Spider.